Supporting Information for:

Mechanism of Voltage Gating in the Voltage-Sensing Phosphatase Ci-VSP

Rong Shen*, Yilin Meng, Benoît Roux, Eduardo Perozo*

Department of Biochemistry and Molecular Biology. The University of Chicago. 929 E 57th Street, Chicago, IL 60637 USA.

This supplementary file includes:

Figs. S1 to **S8**

Materials and Methods

References

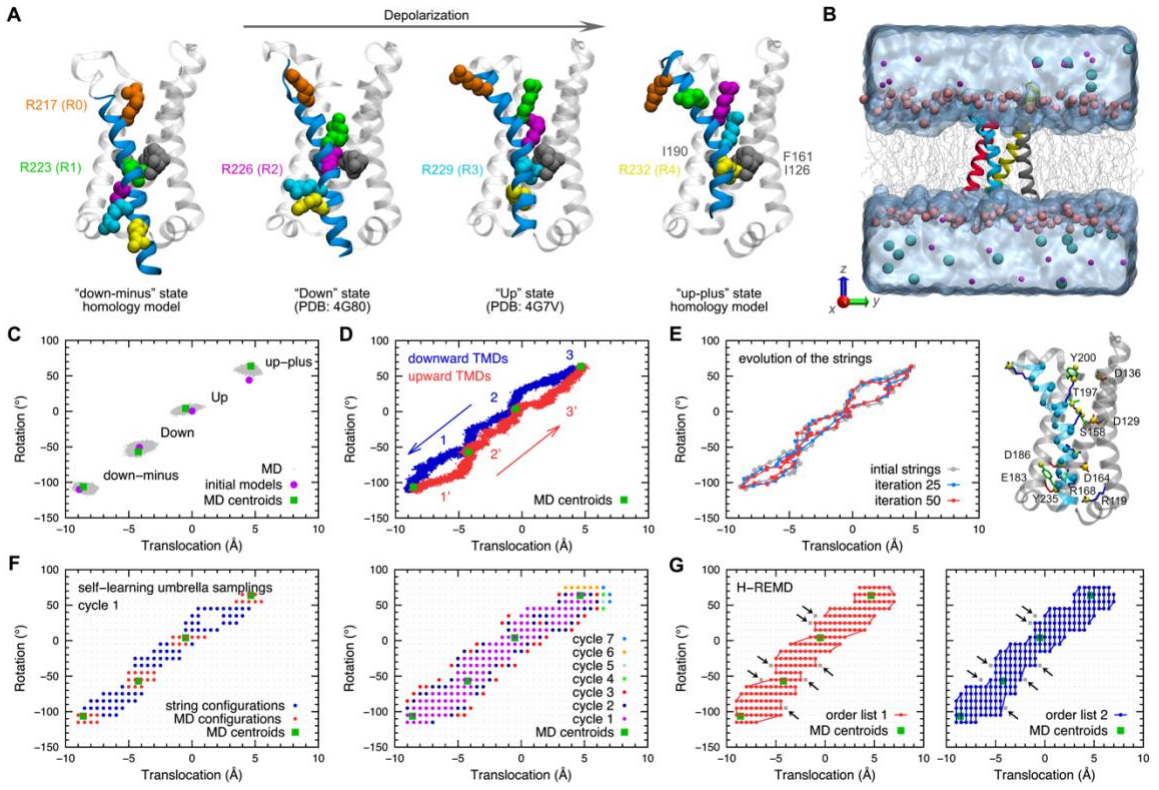

Fig. S1. Workflow for the molecular dynamics (MD) studies of the gating process of the voltage-sensing domain (VSD). (**A**) Starting configurations of the VSD in the "down-minus", "Down", "Up" and "up-plus" states. The arginine residues on S4 and hydrophobic gasket residues (I126, F161 and I190) are shown in vdW representation. (**B**) A MD simulation model of the VSD. The four transmembrane helices are shown in ribbon representation: S1 (gray), S2 (yellow), S3 (red) and S4 (blue); the lipids in gray line representation with the phosphate atoms in pink spheres; bulky water in surface; and ions in spheres. (**C**) Projection of the VSD structures from the last 10 ns trajectory of each MD simulation (n = 5,000, gray dots), the initial models (purple circle) and the centroids of the VSD structures from the last 10 ns trajectory of each MD simulation (green square) into the two reaction coordinates describing the movement of the S4 helix. (**D**) Projection of the VSD structures from the targeted molecular dynamics (TMD) simulations. (**E**) Left, projection of the VSD structure in each of the windows composing the string paths from iterations 0 (gray), 25 (blue) and 50 (red) into the two reaction coordinates, showing the evolution of the string paths connecting the adjacent states. Right, the 36 selected atoms whose Cartesian coordinates having been used as collective variables in the string method are highlighted in spheres. The "Up" state VSD (PDB: 4G7V) is shown in ribbon representation, with the S4 helix being colored in blue for clarity. (**F**) Left, snapshots from the MD simulations (red) and the windows of the string paths (blue) were used as starting configurations for the self-learning umbrella sampling simulations. Right, seven cycles of umbrella sampling simulations were performed. The restraint centers of the umbrella

sampling simulations in each cycle are shown in different colors. (**G**) The two order lists used in the Hamiltonian-replica exchange molecular dynamics (H-REMD) umbrella sampling simulations. Left, the “translocation” is the fast-changing reaction coordinate. Right, the “rotation” is the fast-changing reaction coordinate. The centers of those self-learning umbrella sampling windows that not involved in the H-REMD simulations (7 out of 198) are shown in gray and highlighted by arrows.

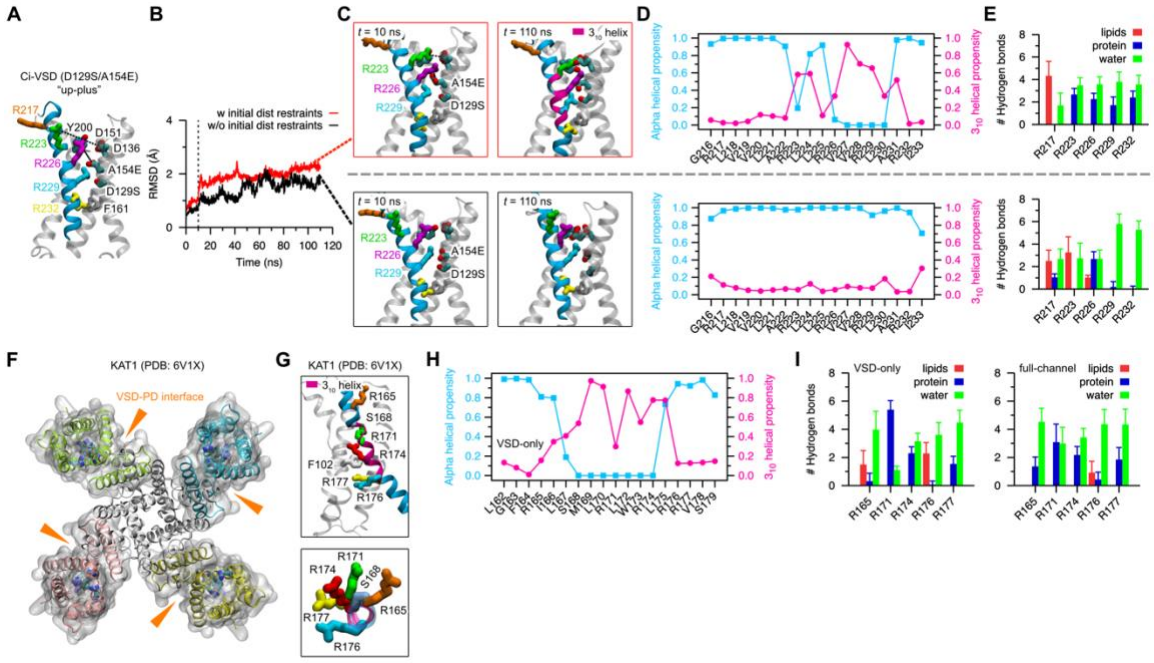

Fig. S2. Secondary structure of the S4 helix. (**A** to **E**) MD simulations of the double-mutant Ci-VSD (D129S/A154E) showing perturbation of the secondary structure of S4 by locations of the countercharges and hydrogen bond interactions between the gating charges and the polar residues and lipid molecules. (**A**) Starting configuration of the double mutant VSD in the "up-plus" state. (**B**) RMSDs of the backbone atoms of the four transmembrane helices in two 110 ns MD simulations. The distances between atoms R226:CZ-E154:CD and R223:CZ-D136:CG, highlighted with dashed lines in (**A**), were harmonically restrained (centered at 5 Å with a force constant of 2 kcal/mol/Å^2) at the first 10 ns of one simulation (red line). (**C**) Snapshots of the VSD taken at time t = 10 ns and 110 ns of the two simulations with (top) and without (bottom) initial distance restraints were shown. The 3_{10} helical region of the S4 helix is colored magenta. (**D**) The alpha helical and 3_{10} helical propensities for S4 residues in the two simulations. (**E**) The average number of hydrogen bonds formed by each of the five arginine residues on S4 with lipid molecules (red), polar residues on S1-S3 (blue) and water molecules (green) in the two simulations. Error bars denote standard deviation. The VSD structures from the last 10 ns trajectory of the simulations were used for the calculation in (**D** and **E**) (n = 1,000). (**F**) Top view of the cryo-EM structure of the KAT1 channel. The S1-S5 helices from different subunits are colored differently with transparent surfaces. (**G**) Close view of the VSD of KAT1. (**H**) The alpha helical and 3_{10} helical propensities for S4 residues of KAT1. The VSD structures from the last 10 ns trajectory of the 50 ns simulation of KAT1 VSD-only system were used for the calculation (n = 1,000). (**I**) The average number of hydrogen bonds formed by the arginine residues on S4 of KAT1 with lipid molecules (red), polar residues on S1-S3 (blue) and water molecules (green) in the simulations with an isolated VSD (left) and a full-channel (right). Error bars denote standard deviation. The snapshots from the last 10 ns

trajectory of the 50 ns simulation of the KAT1 VSD-only system (n = 1,000) and the 40 - 50 ns trajectory of the 500 ns simulation of the KAT1 full-channel system (n = 1,000) were used for the analysis. The VSD and PD interfaces, as shown in (**F**), prevent the formation of hydrogen bond interactions between the gating charges on S4 and the lipid bilayer.

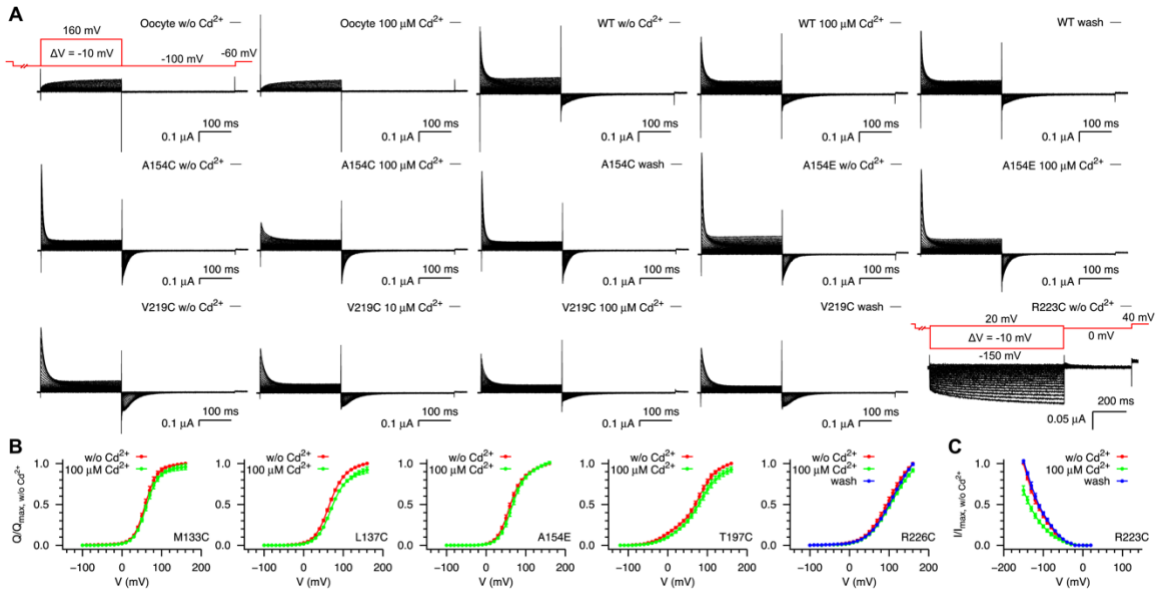

Fig. S3. Functional characterization of wild type and different mutants of Ci-VSP in response to external Cd^{2+} ions. (**A**) Representative currents for non-injected *Xenopus* oocytes and oocytes expressing wild type (WT) and single mutants of Ci-VSP without (w/o), in the presence of, and after washout of extracellular Cd^{2+} ions. A different voltage protocol (inset) was used for Ci-VSP/R223C as omega currents will be elicited at negative voltages for the mutant. (**B**) Representative normalized *Q*-*V* curves for single mutants of Ci-VSP. OFF gating currents were integrated to yield the net translated charge *Q*. The *Q*-*V* curve for each experiment was normalized with respect to the corresponding maximum *Q* measured in the absence of Cd^{2+}. (**C**) Representative normalized *I*-*V* curve for Ci-VSP/R223C. After linear leak subtraction, the *I*-*V* curve for each experiment was normalized with respect to the corresponding maximum current amplitude at the end of the pulses measured in the absence of Cd^{2+}. Error bars denote standard deviation (M133C, n = 4; L137C, n = 5; A154E, n = 3; T197C, n = 4; Y200C, n = 5; R223C, n = 3).

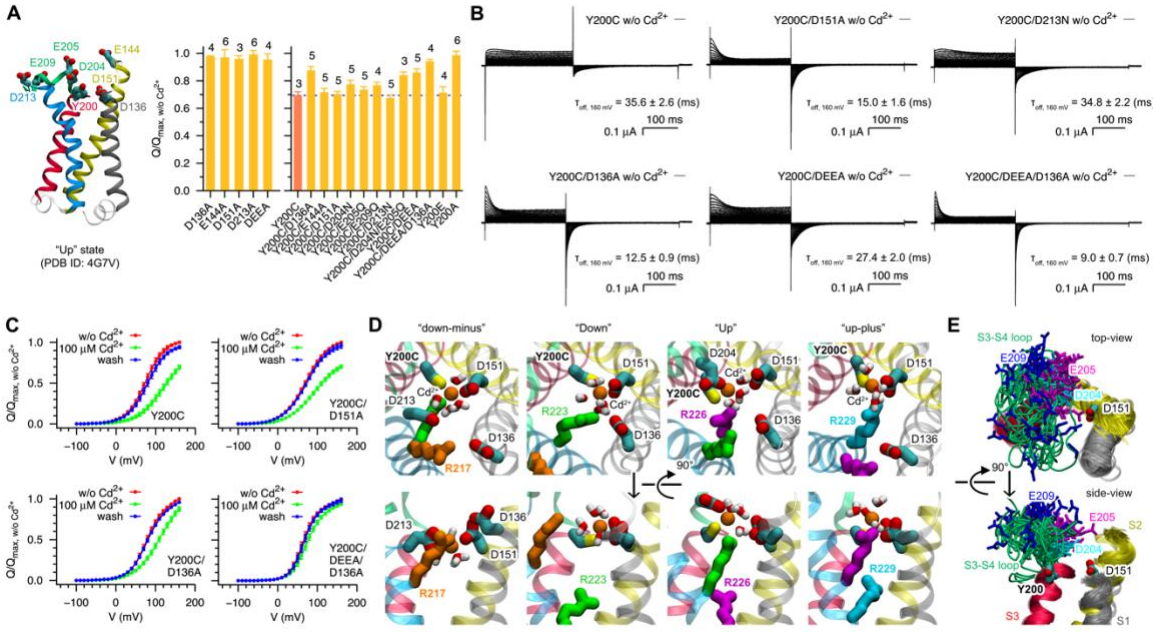

Fig. S4. Cd^{2+} effect on the Y200C mutation at the extracellular side of the S3 helix. (**A**) Left, crystal structure of the "Up" state VSD showing the negatively charged residues surrounding Y200. Right, the relative decreasing of the maximum net off gating charge of Y200C included mutants in response to 100 μM Cd^{2+}. The dashed line represents the mean value of that for the single mutant Y200C as a reference. Error bars denote standard deviation with the number of experiments being listed on the top of each of the bars. (**B**) Representative currents for the mutants of Ci-VSP in the absence of extracellular Cd^{2+} ions. Insets are the time constant (mean ± standard deviation) of the OFF gating current at the voltage pulse of 160 mV. The number of experiments for each construct is listed in (**A**). (**C**) Representative normalized *Q*-*V* curves. (**D**) Top view (top) and side view (bottom) of snapshots from MD simulations of the VSD with the Y200C mutant at the four major states. A Cd^{2+} ion was initially placed at the center of the residues Y200C and D136. Water molecules at the first solvation layer of Cd^{2+} are highlighted in sticks. (**E**) Overlay of snapshots (n = 51) from simulation windows along the minimum free energy path of the H-REMD umbrella sampling simulation at 0 mV. The flexible S3-S4 loop and the three negatively charged residues in it are shown in tube and stick representations, respectively. The S4 helix and the S1-S2 loop are removed for clarity.

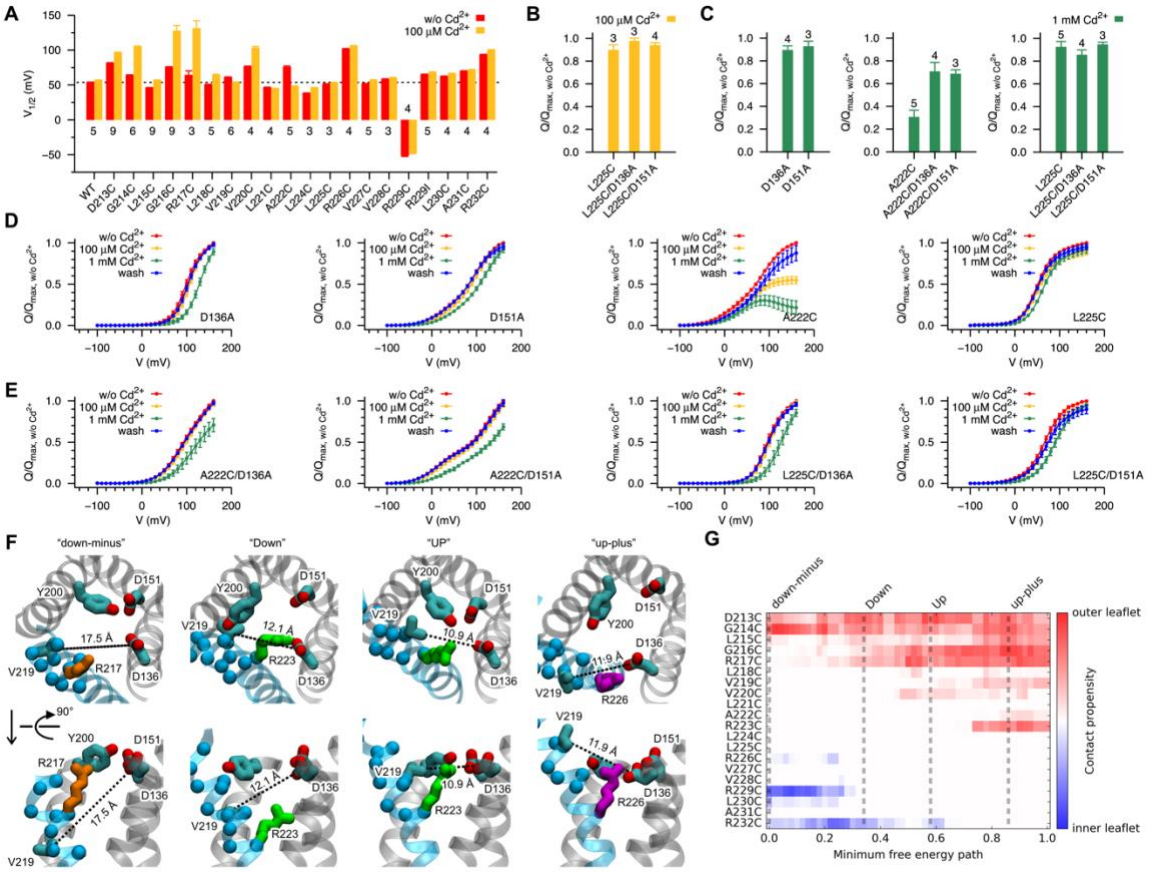

Fig. S5. Single cysteine mutants at the extracellular side of S4 could form Cd^{2+} bridges with the outer leaflet lipid. (**A**) Perturbation of the half-activation voltage ($V_{1/2}$) by single cysteine mutations on S4 and the presence of 100 μM Cd^{2+} in the external recording buffer. (**B** to **E**) The extent of immobilization of S4 is regulated by the external Cd^{2+} concentration and the energetics of gating. (**B**) The relative decreasing of the maximum net OFF gating charge of mutants of Ci-VSP in response to 100 μM Cd^{2+}. (**C**) The relative decreasing of the maximum net OFF gating charge of WT and mutants of Ci-VSP in response to 1 mM Cd^{2+}. (**D**) The normalized *Q*-*V* curves for the WT and single mutants. (**E**) The normalized *Q*-*V* curves for the double mutants. (**F**) Top (top) and side (bottom) view of snapshots of the VSD from MD simulations showing that cysteine mutants at the extracellular side of S4 can hardly form Cd^{2+} bridges with D136. Alpha carbon atoms of residues 213-223 are shown in spheres. The distance between the two atoms V219:CB and D136:CG (connected with a dashed line) in each configuration has been labeled. (**G**) Contact (or Cd^{2+} bridge formation) propensity of S4 residues with the outer and inner leaflets of lipids along the minimum free energy path. The snapshots from the last 5 ns trajectories of simulation windows along the minimum free energy path of the H-REMD umbrella sampling simulation at 0 mV were used for the calculation (n = 50). Residue i is considered to contact to a lipid when the distance between its alpha carbon atom and any one of the nonester phosphate oxygen atoms is below 6 Å.

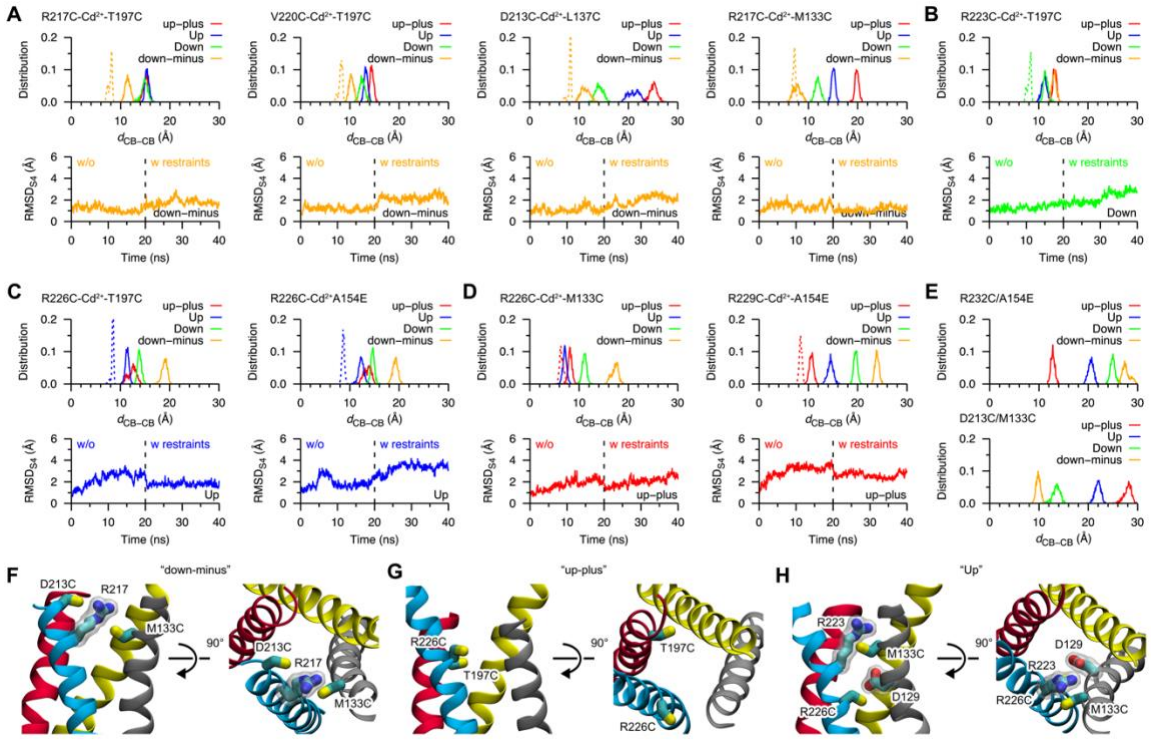

Fig. S6. MD simulations of the double mutants of Ci-VSD with an explicit Cd^{2+} bridge. (**A** to **D**) Top, the distance distribution of the beta carbon atoms of the two mutated residues in each of the 20 ns MD simulations of the Ci-VSD mutants in the "up-plus" (red), "Up" (blue), "Down" (green) and "down-minus" (orange) states (solid line), and in the 20 ns restrained MD simulation of the Ci-VSD mutants in a specific state (the same color scheme) with harmonic restraints on the Cd^{2+} bridge geometry (dashed line). Bottom, the time series of the backbone RMSD of the S4 helix in the MD and restrained MD simulations of the Ci-VSD mutants in the "down-minus" (**A**), "Down" (**B**), "Up" (**C**) and "up-plus" (**D**) states. (**E**) The distance distribution of the beta carbon atoms of the two mutated residues in each of the 20 ns MD simulations of the two double mutants of Ci-VSD (R232C/A514E and D213C/M133C) in different states. These two double mutants cannot form Cd^{2+} bridges in experiments. Snapshots from the last 10 ns trajectory of each simulation were used for the calculation of the distance distributions (n = 1,000). (**F** to **H**) Distance is not the only factor preventing the formation of a Cd^{2+} bridge between two cysteine residues. Intruding of another residue between the two cysteine residues (**F**), impropriate orientation of the side-chain of the two cysteine residues facing away from each other (**G**), and blockage of Cd^{2+} from getting into the middle of the two cysteine residues by other residues (**H**) will all prohibit the formation of a Cd^{2+} bridge even though the two cysteine residues are in an appropriate distance.

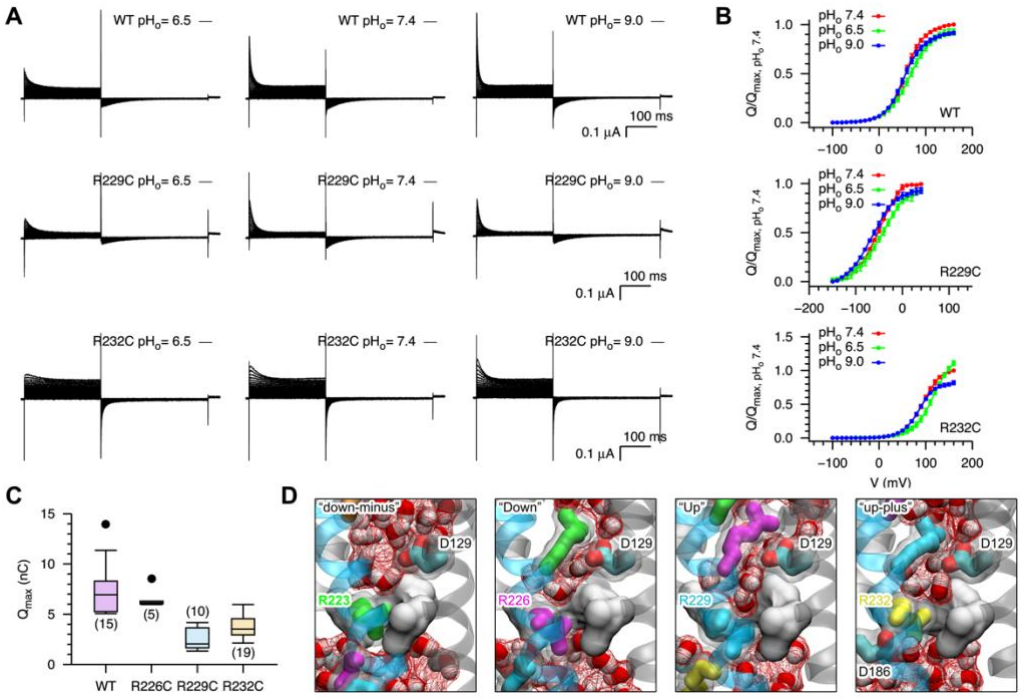

Fig. S7. Determinants preventing the proton leaking through the voltage-sensing domain of Ci-VSP. (**A**) Representative currents for WT, R229C and R232C mutants of Ci-VSP at different pH values (pH_o) of the external recording buffer. (**B**) Normalized *Q*-*V* curves for WT, R229C and R232C mutants of Ci-VSP. The *Q*-*V* curve for each experiment was normalized with respect to the corresponding maximum *Q* measured at pH_o 7.4. Error bars are standard deviation (WT, n = 7, 5, 5 for pH_o 7.4, pH_o 6.5, pH_o 9.0, respectively; R229C, n = 4, 5, 6 for pH_o 7.4, pH_o 6.5, pH_o 9.0, respectively; R232C, n = 4, 9, 6 for pH_o 7.4, pH_o 6.5, pH_o 9.0, respectively). (**C**) Box plot of the maximum net OFF charges of WT, R226C, R229C and R232C mutants of Ci-VSP. The R229C mutant has a smaller Q_{max} compared with the others. The number of experiments for each construct is listed inside the parentheses. (**D**) Snapshots of the WT VSD in the “down-minus”, “Down”, “Up” and “up-plus” states. Water molecules inside the VSD are shown in sticks and wireframe surface representation. The hydrophobic gasket is shown in solid surface representation. The gating charge (R223, R226, R229 or R232) and the surrounding hydrophobic gasket residues form one constriction site, and the countercharge D129 on S1 form the other constriction site by forming salt bridges with the gating charges, to prohibit the formation of a continuous water wire connecting the two sides of the VSD, thus prevent the proton leaking during the gating process.

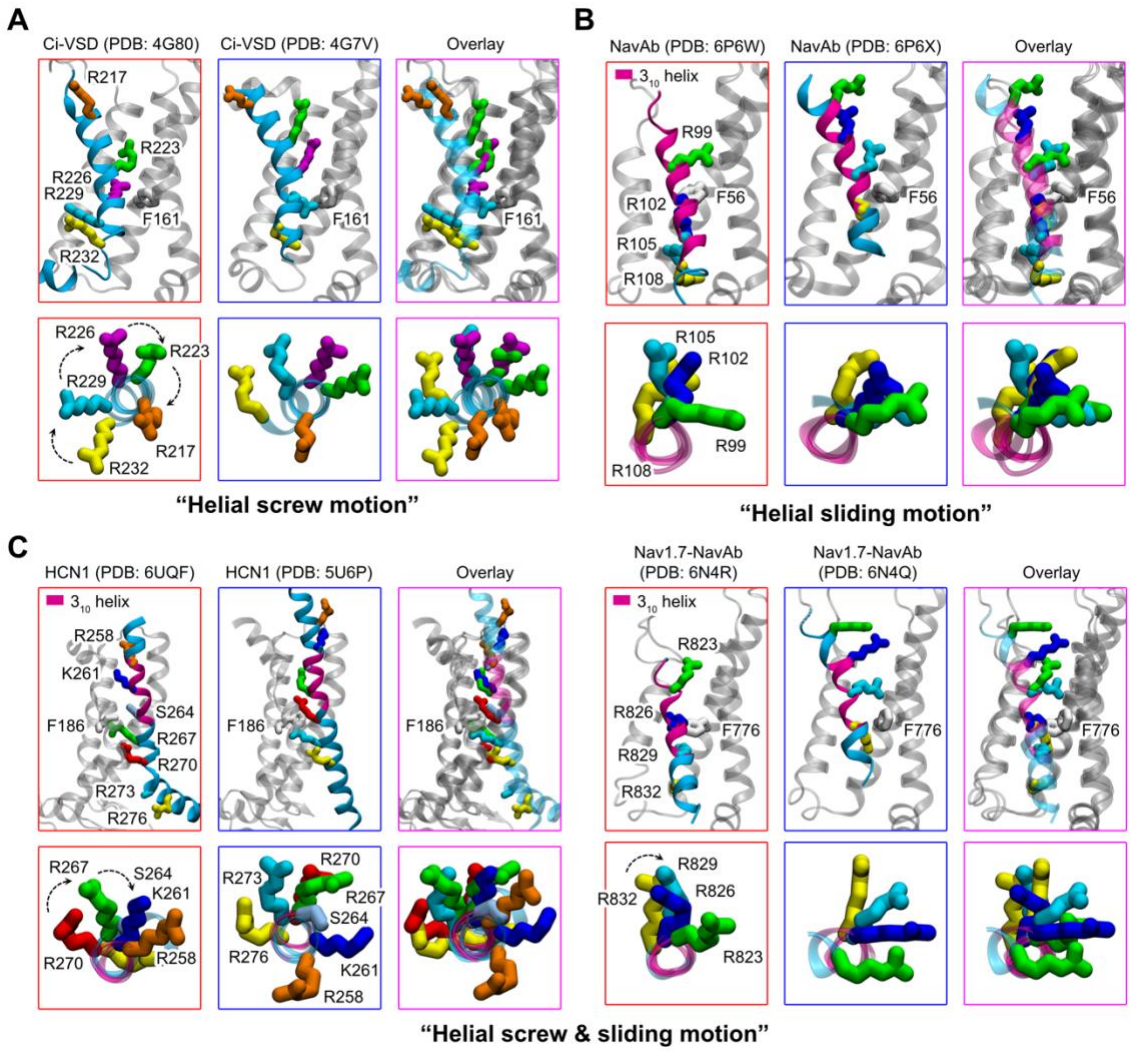

Fig. S8. Proposed gating mechanisms in different types of voltage-sensing domains. (**A**) Crystal structures of the VSD of Ci-VSP at two different states. (**B**) Cryo-EM structures of the VSD of the NavAb channel at two different states. (**C**) Cryo-EM structures of the VSD of the HCN1 channel and the Nav1.7-NavAb chimera channel at two different states. The dashed arrows in the top view of the S4 helices (bottom panels in **A** and **C**) represent approximate rotating motions of certain positively charged residues during the gating process. The 3_{10} helical parts of the helices are colored in magenta. S4 residues in the alpha helical and 3_{10} helical conformations will undergo helical screw and helical sliding motions during gating, respectively.

Materials and Methods

Simulation systems

The crystal structures of the “Up” (PDB: 4G7V) and “Down” (PDB: 4G80) states Ci-VSD (*1*) were used as templates to build the “up-plus” and “down-minus” states homology models. Based on the structural alignment of the “Up” and “Down” states Ci-VSD and the one helix turn (three-residue) or one ‘click’ model (*1*), the S4 helix of the “up-plus” and “down-minus” states VSD was shifted 3 residues upward and 6 residues downward, respectively, compared with the “Up” state Ci-VSD in the sequence alignment step of homology modeling. Then, the program MODELLER (*2*) was used for the structure building of the homology models. For consistency, the four models have the same number of residues: 106−239, with the C-terminal end of the S4 helix being modeled as a continuous helix (Fig. S1A). The R217E mutation in the “Up” state crystal structure was reversed and its missing residues: 237−239 at the C-terminal end were rebuilt.

The “Up” state Ci-VSD was embedded into a palmitoyl oleyl phosphatidylcholine (POPC) lipid bilayer fully solvated in 0.1 M NaCl using the program VMD (*3*). Titratable residues were assigned their default protonation state at pH 7. The orientation and relative positive of the protein inside the membrane was adjusted according to the prediction from the orientations of proteins in membranes (OPM) database (*4*) The protein was substituted into one of the other three states Ci-VSD to construct the other three systems. The resulting four systems were electrically neutral and consisted of the same components with a total number of atoms of 56,582 (Fig. S1B).

Molecular dynamics simulations

The systems underwent 1,000 steps of initial energy minimization followed by 30 ns and 60 ns equilibration runs for the “Up” and “Down” systems and the “up-plus” and “down-minus” systems, respectively. The homology model structures were equilibrated 30 ns longer for better relaxation of the systems. During the equilibration runs, positions of the protein heavy atoms were harmonically restrained with the force constant being gradually decreased (*5*). After the equilibration run, 20 ns production run was carried out for each of the four systems (Fig. S1C).

Targeted molecular dynamics simulations

Targeted molecular dynamics (TMD) simulations were performed to generate initial transition pathways between two adjacent states (Fig. S1D). The centroids of the structures of the four systems from the last 10 ns production runs (n = 5,000) were used as starting and targeting configurations for the upward and downward TMD simulations. The Cartesian coordinates of the non-hydrogen atoms of the four transmembrane helices (residues: 116−138, 144−172, 181−202 and 216−236) were used in hierarchical cluster analysis to get the centroids (*6*). All the heavy atoms of the protein were chosen as targeted atoms. Each TMD simulation lasted 10 ns with a spring constant of 200

kcal/mol/Å^2 following 1,000 steps of energy minimization.

String method with swarms of trajectories

The string method with swarms of trajectories with MD simulations was used to characterize and relax the transition pathways derived from the TMD simulations. Six strings connecting the four centroids of the structures from MD simulations were constructed and evolved for 50 iterations (Fig. S1E). Each string contained a chain of 12 images or states. The initial configurations for the intermediate images were taken from the TMD simulations. The Cartesian coordinates of the C_α atoms of S4 residues: 216−235, and one representative side-chain atom of a group of key residues: the CG atoms of D129, D136, D164 and D186; the CD atom of E183; the CZ atoms of R119, R168, R217, R223, R226, R229 and R232; the OH atoms of Y200 and Y235; the OG atom of S158; the OG1 atom of T197, were selected as collective variables (Fig. S1E). During the iteration, 20 short MD simulations (5 ps/trajectory) with different initial velocities were launched for each of the 10 intermediate images of each string. Protein structures from the last frame of the 20 trajectories of each image were then aligned, averaged and reparametrized. The resulting structure was used as the starting configuration of the image for the next iteration by a 150 ps equilibration run with collective variables being harmonically restrained (with a gradually increased force constant up to 20 kcal/mol/Å^2) following an energy minimization of 1,000 steps (*7*).

Self-learning adaptive umbrella sampling

We used the umbrella sampling method (*8*, *9*) to calculate the free energy landscape or potential of mean force (PMF) for the conformational change of Ci-VSD during the gating process. Two reaction coordinates, defined using the collective variables interface (Colvars) module (*10*) in NAMD, were employed to describe the translocation and rotation of the S4 helix: *distanceZ*, projection of the distance vector between the center of mass of the C_α atoms of residues: 217−233 and a reference point (the center of mass of the C_α atoms of residues: 217−233 in the “Up” state crystal structure) along a constant vector (the principle axis of the C_α atoms of residues: 217−233 in the “Up” state crystal structure); and *spinAngle*, angle of the spin rotation of the C_α atoms of residues: 217−233 in reference to the positions of these atoms in the “Up” state crystal structure, along and around its axial axis, respectively.

To improve the efficiency of the umbrella sampling, we used the self-learning adaptive umbrella sampling approach (*11*), which can explore the free energy landscape of a multi-dimensional space and find the most relevant and worth sampling regions automatically. It helps us put our efforts and computing resources on the most important subspace instead of the irrelevant high free energy regions, thus decreasing the total number of umbrella sampling windows significantly.

Snapshots from the last 10 ns production MD runs (n = 38) and the last ten iterations of the string method (n = 74) were used as starting configurations for the first cycle of the

self-learning adaptive umbrella sampling simulations (Fig. S1F). The umbrella sampling widow increments for the two reaction coordinates were 0.5 Å and 10 °, and the force constants for the two restraints were 5.0 kcal/mol/Å^2 and 0.02 kcal/mol/deg^2, respectively. To prevent global drifting of the protein, the projection of the center of mass of the C_α atoms of the S1-S3 helices (residues: 116−138, 144−172 and 181−202) in the *xy* plane and the projection of the center of mass of the phosphate atoms of lipids along the ***z*** axis were also restrained with a force constant of 5.0 kcal/mol/Å^2. A free energy value of 10 kcal/mol was used as the threshold, and a total of seven cycles of 198 windows were generated. For each umbrella sampling window, a 20 ns production run was carried out following a 5 ns equilibration run with the root-mean-square deviation of the C_α atoms of the four transmembrane helices with respect to the starting configuration (with a force constant of 50.0 kcal/mol/Å^2) and the orientation of the C_α atoms of the first three helices in reference to that in the "Up" state crystal structure (with a force constant of 10.0 kcal/mol) being also restrained. The weighted histogram analysis method (WHAM) was used to combine the sampling data and calculate the PMF (*12*). The WHAM code was obtained by courtesy of Dr. Sunhwan Jo.

Hamiltonian-replica exchange molecular dynamics (H-REMD) umbrella sampling at different membrane potentials

The landscape or the subspace explored by the self-learning adaptive umbrella sampling simulations was used in the H-REMD umbrella sampling simulations. Two one-dimensional ordered lists of umbrella sampling windows were generated to assign exchanging partners for each replica (Fig. S1G). To keep the Euclidean distance between two exchanging replicas as short as possible (*13*), we used 191 out of 198 windows derived from the self-learning adaptive umbrella sampling simulations. For the H-REMD simulations at 0 mV (no membrane potential exist), snapshots of the last frame of the selected windows from the self-learning adaptive umbrella sampling simulations were used as starting configurations directly. The reaction coordinates and restraints were the same as those in the self-learning adaptive umbrella sampling simulations. The simulations were carried out for 30 ns with an exchange attempt rate of 1 ps^{-1}. For the H-REMD simulations at ±150 mV, the 191 selected self-learning adaptive umbrella sampling windows were re-simulated using the same protocol under the assigned membrane potential. The resulting configurations were used as starting structures for the 30 ns H-REMD simulations. The membrane potential was applied using the external electric field module of NAMD in which the electric field $E = V/L_z$, where V is the voltage and L_z is the length of the box in the z direction scaled by the cell basis vectors (*14*). The PMFs for the H-REMD umbrella sampling simulations were also calculated via the WHAM method. The minimum free energy path connecting the local free energy minima was calculated using the zero temperature string method (*15*). The average displacement charge for each sampling window was calculated as $Q_\mathrm{d} = \langle \sum_i q_i z_i / L_z \rangle$, using the partial charge q_i and unwrapped z_i coordinate of all atoms of the system from the last 5 ns trajectories of the H-

REMD simulations (*14*, *16*).

Molecular dynamics simulations of the "up-plus" state Ci-VSD with countercharge mutations

A double mutation (D129S/A154E) model of Ci-VSD was constructed using the program VMD based on the "up-plus" state centroid structure from the MD simulation (Fig. S2A). Two sets of MD simulations were performed to display the effect of the double mutation on the secondary structure conformation of the S4 helix. In one of the simulation, the distances between the atoms R226:CZ−E154:CD and R223:CZ−D136:CG were harmonically restrained (centered at 5 Å with a force constant of 5.0 kcal/mol/Å^2) in addition to the positional restraints on the backbone atoms of the S1-S3 helices (a force constant of 1.0 kcal/mol/Å^2) in the initial 10 ns equilibration run, followed by a 100 ns production run without any restraints. In the other simulation, the same simulation protocol was used except that the distance restraints between the two atom pairs were not implemented in the equilibration run.

Molecular dynamics simulations of the Y200C and V220C mutants

The Y200C mutation was carried out on the centroid structures of the four systems at different states using VMD. The newly introduced cysteine residue was modeled in a deprotonated state (*17*) carrying a net charge of -1 e. A Cd^{2+} ion was also added into each of the four systems (Fig. S4D). Following 5,000 steps of energy minimization, a 5 ns equilibration run and a subsequent 10 ns production run were performed for each system. During the equilibration run, the positions of the backbone atoms of the protein and the Cd^{2+} ion initially at the center of C200:SG and D136:CG were harmonically restrained, with a force constant of 5.0 and 1.0 kcal/mol/Å^2, respectively.

The V220C mutant was constructed on the centroid structure of the "up-plus" state Ci-VSD using VMD. The modeling and simulation protocols were the same as the Y200C mutant, except that the Cd^{2+} was inserted between the side-chain of V200C and the phosphate atom of a nearby lipid molecule.

Restrained molecular dynamics simulations with an explicit Cd^{2+} bridge

To explicitly simulate the Cd^{2+} bridges and assess the corresponding state they are associated with (*18*), we constructed 11 double mutants of Ci-VSD in all of the four states using the centroid structures from the MD simulations with the program VMD: R217C/T197C, V220C/T197C, V220C/L137C, R223C/T197C, R226C/T197C, D213C/L137C, R226C/L137C, R217C/M133C, R226C/M133C, R226C/A154E and R229C/A154E. In addition, we constructed two more double mutants that incapable of forming Cd^{2+} bridges in our electrophysiology experiments to study the underlying molecular mechanism: R232C/A154E and D213C/M133C.

Each double mutant system was simulated for 20 ns following 5,000 steps energy minimization. The distance distribution between the C_β atoms of the two mutated residues

was calculated and analyzed together with the MD trajectory. The states in which the Cd^{2+} bridge could form were selected for the restrained MD simulation. Snapshots of the last frame of the selected trajectories were chosen to construct starting configurations for the restrained MD simulations by deprotonating the introduced cysteine residue(s) and inserting a Cd^{2+} ion between the two mutated residues using the program VMD. Each restrained MD simulation was run for 20 ns following 5,000 steps energy minimization, with the geometry of the Cd^{2+} bridge being harmonically restrained (*17*, *18*).

Hydration of the crevices of Ci-VSD

Single cysteine mutation of the four gating-charge residues on S4: R223C, R226C, R229C and R232C at different states were built based on the centroid structures from the previous MD simulations using the program VMD. Each system was run for 50 ns following 5,000 steps energy minimization. The breadth-first algorithm was used to find a continuous hydrogen-bonded water wire connecting the extracellular and intracellular sides of the VSD (*19*). Two water molecules were considered to form a hydrogen bond when the distance between the two oxygen atoms was shorter than 3.5 Å and the angle between the donor oxygen atom, the shared hydrogen atom and the acceptor oxygen atom was larger than 120 °.

The latterly constructed systems with mutations were all neutralized, by changing the ion composition in the bulky water, if the net charge of the systems were not zero. All MD simulations were performed using NAMD (*20*) with a time step of 2 fs. The CHARMM36 force field (*21*, *22*) including the CMAP correction was used for the protein, lipids and ions, and the TIP3P model (*23*) for water. The Langevin dynamics and the Nose-Hoover Langevin piston method (*24*, *25*) were employed to control the temperature at 300 K and the pressure at 1 atm, respectively. The long range electrostatic interactions were calculated using the particle mesh Ewald (PME) method (*26*) with a grid density of at least $1/Å^3$. A smoothing switch function was applied for the van der Waals interactions starting from the distance of 10 Å and with a cutoff of 12 Å.

Molecular biology

The catalytically inactive mutant of Ci-VSP (C363S) (*27*) was used as background for all the mutations and gating currents recordings, hereafter referred to as the “wild type” (“WT”) Ci-VSP. The cDNA of Ci-VSP-C363S was cloned into the pSP64T vector. All point mutations were generated using site-directed mutagenesis and confirmed by further sequencing. For all single and double cysteine mutants, the native cysteine on the voltage-sensing domain was also mutated to a serine (C159S). The plasmids containing WT or mutant Ci-VSP were linearized by restriction enzyme XbaI. cRNA was transcribed *in vitro* using the mMessage mMachine SP6 transcription kit (Ambion, Invitrogen) and diluted in RNase-free water in a concentration of approximately 1 µg/µL.

Xenopus laevis oocytes were surgically harvested and defolliculated using collagenase solution with bovine serum albumin (BSA). Each freshly isolated oocyte was

injected with 50 nL of cRNA. Injected oocytes were incubated for 16–24 hours at 18 °C in standard oocyte saline (SOS) solution containing the following components: 100 mM NaCl, 5 mM KCl, 2 mM $CaCl_2$, 1mM $MgCl_2$, 10 mM HEPES at pH 7.4, and 50 μg/ml gentamycin. For the various cysteine mutants, 0.5 mM dithiothreitol (DTT) was added into the incubation solution to prevent formation of disulfide bond (*28*) and chelate heavy metal contaminants from water and/or chemicals (*29*, *30*).

Electrophysiological recordings and data analysis

Gating currents were recorded at room temperature (20–23 °C) on a cut-open oocyte voltage-clamp setup (*31*, *32*). Raw currents were filtered at 10 kHZ with a low pass four-pole Bessel filter within the CA-1 amplifier (Dagan Corporation; Minneapolis, MN). The ON and OFF currents were evoked using the following voltage protocol: in brief, from a holding potential of -60 mV, a 200 ms conditioning prepulse to -100 mV was applied to maximally deactivate Ci-VSP. Then, 250 ms depolarization voltage steps from 160 mV to -100 mV in -10 mV decrements were applied to initiate the ON currents, followed by a 350 ms repolarization potential to -100 mV to measure the OFF currents. Due to the presence of non-negligible endogenous outward currents at potentials more positive than 40 mV (*33*), with subtle inward currents upon returning to very negative potentials (Fig. S3A), we used the net OFF charge to represent the total charge movement Q which was calculated by time integration of the OFF gating current. For mutants whose gating charge starts moving at more negative potentials, the prepulse and repolarization potentials and the minimum test pulse were changed correspondingly to more negative potentials (e.g., R229C to -140 mV). For mutants involving the R223C mutation which conduct omega currents at polarization states (*34*, *35*), preceded by a 200 ms prepulse to 0 mV, 800 ms voltage steps from 20 mV to -150 mV were applied to evoke the currents followed by a 400 ms voltage step to 0 mV, and the holding potential was 40 mV. The steady-state current amplitudes I were used to study the functional property of the mutants. Leak and fast transient capacitive currents were subtracted offline. Data acquisition and analysis were performed using in-house software GPatch and Analysis, respectively, kindly provided by Prof. Francisco Bezanilla.

The external solution contained (in mM): 120 N-methyl-D-glucamine (NMDG), 2 $Ca(OH)_2$, 0.5 EDTA and 10 buffering agent: HEPES for pH7.4, MES for pH6.0 and CHES for pH9.0. The internal solution contained (in mM): 120 NMDG, 2 EGTA, and 10 HEPES at pH7.4. Methanesulfonic acid was used for pH adjustment. When needed, Cd^{2+} was diluted in the external solution without EDTA at designed concentration from a 100 mM $CdCl_2$ stock solution (*36*). 1~2 mM DTT was freshly added to the external solution to chelate/washout the Cd^{2+} ions.

The normalized net OFF charge-voltage (Q–V) curves for each construct and condition (extracellular recording solution) were averaged and fitted with a Boltzmann distribution, $Q(V)=1/\{1+\exp[ze_0(V-V_{1/2})/k_BT]\}$, where z is the apparent gating charge, $V_{1/2}$ is the half activation voltage, e_0 is the elementary charge, k_B is the Boltzmann constant

and T is the absolute temperature in Kelvin. The python scipy.optimize.curve_fit procedure was used for fitting and calculating the best-fit values and standard deviations for the parameters z and $V_{1/2}$. The OFF gating currents were fitted to a sum of two independent exponential functions, and a weighted mean time constant, $\tau_{OFF} = (A_1\tau_1 + A_2\tau_2)/(A_1+A_2)$, was used to characterized the kinetics of deactivation, where A_1, A_2 and τ_1, τ_2 are the amplitudes and time constants for the first and second exponentials, respectively. The effective Cd^{2+} effect on the maximum normalized net OFF charge of the double mutants, with respect to the maximum net OFF charge in the absence of Cd^{2+}, was calculated by subtracting the corresponding Cd^{2+} effect on each single mutant from that of the double mutant, $\Delta\Delta Q_{ij}/Q_{ij,\ max,\ w/o\ Cd^{2+}} = |Q_{ij}/Q_{ij,\ max,\ w/o\ Cd^{2+}} - Q_i/Q_{i,\ max,\ w/o\ Cd^{2+}} * Q_i/Q_{i,\ max,\ w/o\ Cd^{2+}}|$, with the standard deviation being estimated using the rule of linear propagation of uncertainty (*37*).

References

1. Q. Li, S. Wanderling, M. Paduch, D. Medovoy, A. Singharoy, R. McGreevy, C. A. Villalba-Galea, R. E. Hulse, B. Roux, K. Schulten, A. Kossiakoff, E. Perozo, Structural mechanism of voltage-dependent gating in an isolated voltage-sensing domain. *Nat Struct Mol Biol*. 21, 244–252 (2014).
2. A. Šali, T. L. Blundell, Comparative Protein Modelling by Satisfaction of Spatial Restraints. *J Mol Biol*. 234, 779–815 (1993).
3. W. Humphrey, A. Dalke, K. Schulten, VMD: Visual molecular dynamics. *J Mol Graphics*. 14, 33–38 (1996).
4. M. A. Lomize, I. D. Pogozheva, H. Joo, H. I. Mosberg, A. L. Lomize, OPM database and PPM web server: resources for positioning of proteins in membranes. *Nucleic Acids Res*. 40, D370–D376 (2012).
5. R. Shen, W. Guo, W. Zhong, Hydration valve controlled non-selective conduction of Na^+ and K^+ in the NaK channel. *Biochimica et Biophysica Acta - Biomembr*. 1798, 1474–1479 (2010).
6. Y. Meng, C. Gao, D. K. Clawson, S. Atwell, M. Russell, M. Vieth, B. Roux, Predicting the Conformational Variability of Abl Tyrosine Kinase using Molecular Dynamics Simulations and Markov State Models. *J Chem Theory Comput*. 14, 2721–2732 (2018).
7. W. Gan, S. Yang, B. Roux, Atomistic View of the Conformational Activation of Src Kinase Using the String Method with Swarms-of-Trajectories. *Biophys J*. 97, L8–L10 (2009).
8. G. M. Torrie, J. P. Valleau, Nonphysical sampling distributions in Monte Carlo free-energy estimation: Umbrella sampling. *J Comput Phys*. 23, 187–199 (1977).
9. R. Shen, W. Guo, Mechanism for Variable Selectivity and Conductance in Mutated NaK Channels. *J Phys Chem Lett*. 3, 2887–2891 (2012).
10. G. Fiorin, M. L. Klein, J. Hénin, Using collective variables to drive molecular dynamics simulations. *Mol Phys*. 111, 3345–3362 (2013).
11. W. Wojtas-Niziurski, Y. Meng, B. Roux, S. Bernèche, Self-Learning Adaptive Umbrella Sampling Method for the Determination of Free Energy Landscapes in Multiple Dimensions. *J Chem Theory Comput*. 9, 1885–1895 (2013).
12. S. Kumar, J. M. Rosenberg, D. Bouzida, R. H. Swendsen, P. A. Kollman, THE weighted histogram analysis method for free-energy calculations on biomolecules. I. The method. *J Comput Chem*. 13, 1011–1021 (1992).
13. W. Jiang, J. C. Phillips, L. Huang, M. Fajer, Y. Meng, J. C. Gumbart, Y. Luo, K. Schulten, B. Roux, Generalized scalable multiple copy algorithms for molecular dynamics simulations in NAMD. *Comput Phys Commun*. 185, 908–916 (2014).
14. B. Roux, The Membrane Potential and its Representation by a Constant Electric Field in Computer Simulations. *Biophys J*. 95, 4205–4216 (2008).

15. L. Maragliano, A. Fischer, E. Vanden-Eijnden, G. Ciccotti, String method in collective variables: Minimum free energy paths and isocommittor surfaces. *J Chem Phys*. 125, 024106 (2006).
16. F. Khalili-Araghi, V. Jogini, V. Yarov-Yarovoy, E. Tajkhorshid, B. Roux, K. Schulten, Calculation of the Gating Charge for the Kv1.2 Voltage-Activated Potassium Channel. *Biophys J*. 98, 2189–2198 (2010).
17. R. Shen, W. Han, G. Fiorin, S. M. Islam, K. Schulten, B. Roux, Structural Refinement of Proteins by Restrained Molecular Dynamics Simulations with Non-interacting Molecular Fragments. *Plos Comput Biol*. 11, e1004368 (2015).
18. E. Vargas, F. Bezanilla, B. Roux, In Search of a Consensus Model of the Resting State of a Voltage-Sensing Domain. *Neuron*. 72, 713–720 (2011).
19. W. Han, R. C. Cheng, M. C. Maduke, E. Tajkhorshid, Water access points and hydration pathways in CLC H^+/Cl^- transporters. *Proc National Acad Sci*. 111, 1819–1824 (2014).
20. J. C. Phillips, R. Braun, W. Wang, J. Gumbart, E. Tajkhorshid, E. Villa, C. Chipot, R. D. Skeel, L. Kalé, K. Schulten, Scalable molecular dynamics with NAMD. *J Comput Chem*. 26, 1781–802 (2005).
21. A. D. M. Jr, D. Bashford, M. Bellott, R. L. D. Jr, J. D. Evanseck, M. J. Field, S. Fischer, J. Gao, H. Guo, S. Ha, D. Joseph-McCarthy, L. Kuchnir, K. Kuczera, F. T. K. Lau, C. Mattos, S. Michnick, T. Ngo, D. T. Nguyen, B. Prodhom, W. E. R. III, B. Roux, M. Schlenkrich, J. C. Smith, R. Stote, J. Straub, M. Watanabe, J. Wiórkiewicz-Kuczera, D. Yin, M. Karplus, All-Atom Empirical Potential for Molecular Modeling and Dynamics Studies of Proteins. *J Phys Chem B*. 102, 3586–3616 (1998).
22. A. D. MacKerell, M. Feig, C. L. Brooks, Improved treatment of the protein backbone in empirical force fields. *J Am Chem Soc*. 126, 698–9 (2004).
23. W. L. Jorgensen, J. Chandrasekhar, J. D. Madura, R. W. Impey, M. L. Klein, Comparison of simple potential functions for simulating liquid water. *J Chem Phys*. 79, 926–935 (1983).
24. G. J. Martyna, D. J. Tobias, M. L. Klein, Constant pressure molecular dynamics algorithms. *J Chem Phys*. 101, 4177–4189 (1994).
25. S. E. Feller, Y. Zhang, R. W. Pastor, B. R. Brooks, Constant pressure molecular dynamics simulation: The Langevin piston method. *J Chem Phys*. 103, 4613–4621 (1995).
26. U. Essmann, L. Perera, M. L. Berkowitz, T. Darden, H. Lee, L. G. Pedersen, A smooth particle mesh Ewald method. *J Chem Phys*. 103, 8577–8593 (1995).
27. Y. Murata, H. Iwasaki, M. Sasaki, K. Inaba, Y. Okamura, Phosphoinositide phosphatase activity coupled to an intrinsic voltage sensor. *Nature*. 435, 1239–1243 (2005).
28. U. Henrion, J. Renhorn, S. I. Börjesson, E. M. Nelson, C. S. Schwaiger, P. Bjelkmar, B. Wallner, E. Lindahl, F. Elinder, Tracking a complete voltage-sensor cycle with metal-ion bridges. *Proc National Acad Sci*. 109, 8552–8557 (2012).

29. V. V. Cherny, V. S. Markin, T. E. DeCoursey, The voltage-activated hydrogen ion conductance in rat alveolar epithelial cells is determined by the pH gradient. *J Gen Physiology*. 105, 861–896 (1995).
30. A. Krężel, W. Leśniak, M. Jeżowska-Bojczuk, P. Młynarz, J. Brasuñ, H. Kozłowski, W. Bal, Coordination of heavy metals by dithiothreitol, a commonly used thiol group protectant. *J Inorg Biochem*. 84, 77–88 (2001).
31. M. Taglialatela, L. Toro, E. Stefani, Novel voltage clamp to record small, fast currents from ion channels expressed in Xenopus oocytes. *Biophys J*. 61, 78–82 (1992).
32. E. Stefani, F. Bezanilla, [17] Cut-open oocyte voltage-clamp technique. *Methods Enzymol*. 293, 300–318 (1998).
33. A. Vasilyev, E. Indyk, R. F. Rakowski, Properties of a Sodium Channel (Nax) Activated by Strong Depolarization of Xenopus Oocytes. *J Membr Biology*. 185, 237–247 (2002).
34. D. M. Starace, F. Bezanilla, A proton pore in a potassium channel voltage sensor reveals a focused electric field. *Nature*. 427, 548–553 (2004).
35. F. Tombola, M. M. Pathak, P. Gorostiza, E. Y. Isacoff, The twisted ion-permeation pathway of a resting voltage-sensing domain. *Nature*. 445, 546–549 (2007).
36. C. A. Z. Bassetto, J. L. Carvalho-de-Souza, F. Bezanilla, Metal Bridge in S4 Segment Supports Helix Transition in Shaker Channel. *Biophys J*. 118, 922–933 (2020).
37. O. Yifrach, R. MacKinnon, Energetics of Pore Opening in a Voltage-Gated K^+ Channel. *Cell*. 111, 231–239 (2002).